Environmental Influence on Module Delamination Rate

Nick Bosco, Jared Tracy, and Reinhold Dauskardt

***Abstract*—This study begins to investigate the role of environmental factors, such as temperature and humidity, on the delamination kinetics of the ethylene vinyl acetate (EVA)/silicon–photovoltaic (Si–PV) cell interface. A fracture mechanics approach based on a single cantilever beam technique is employed to measure the delamination rate as a function of applied driving force. To glean insight into the mechanisms of bonding and degradation at this interface, and the effect of manufacturing variability and quality, we consider a high-quality pristine EVA and two EVAs formulated with reduced amounts of its adhesion promoter, silane. Results indicate that a bulk change in the viscoelastic properties of the EVA dominates the delamination kinetics at high driving forces and low humidity and the effect of a chemical reaction only becomes apparent at higher humidity and lower driving forces. These findings suggest that only interfacial phenomenon of susceptible, degraded material may have to be considered to adequately model PV module delamination failure.**

***Index Terms*—Accelerated aging, adhesive strength, delamination, materials reliability, photovoltaic cells.**

I. Introduction

RECENT studies have begun to quantify the critical strain energy release rate, G_C, at the encapsulant/silicon photovoltaic cell (Si–PV) interface in both new and exposed modules [1]–[4]. While values of 2500–3000 J/m^2 are expected for a quality ethylene vinyl acetate (EVA)/Si–PV interface, one study found that delamination was only observed in modules (fielded up to 26 years) when their G_C values were below 160 J/m^2 [2]. Because EVA delamination failures are still observed, however, it suggests that either initial quality or environmental degradation can severely compromise the adhesion of this interface [5], [6].

Delamination in a PV module will occur when the debond driving force, G, exceeds G_C. Because G_C decreases with increasing temperature, and G will develop due to thermomechanical strain in the module, delamination is likely to occur when the module is at elevated temperatures. However, a complicating matter is *subcritical debonding*: when delamination occurs at a finite rate at driving forces below G_C. This phenomenon may occur in the EVA/Si–PV system due to the viscoelastic behavior of the encapsulant and/or stress-enabled chemical reactions with environmental species, such as water [7], [8]. Typically, the debonding rate due to viscoelastic behavior results in a characteristic sigmoidal curve on a v-G plot: debond growth rate versus applied driving force, Fig. 1. Here, the curve is bound by G_C at very fast debonding rates, and a threshold value of debond driving force, G_{TH}, below which the delamination front will arrest [9]. Between these limiting values (region I), the response is often fitted by a power law relationship that, for instance, will shift due to the influence temperature on deformation of the material at the debond front. Subcritical debonding due to reaction with environmental species, also known as environmentally assisted debonding, results in a similar debond growth rate curve where a chemical reaction at the debond front will result in characteristic region I behavior where the debond growth rate is controlled by the applied driving force. If, however, the rate limiting step becomes diffusion of the reactive species to the debond front, a characteristic transport-controlled region II will emerge that is relatively insensitive to the applied debond driving force.

In the present study, we begin to investigate the kinetics of subcritical debonding at the EVA/Si–PV interface. To probe the mechanisms of bonding and degradation at this interface, and the effect of manufacturing variability and quality, we have

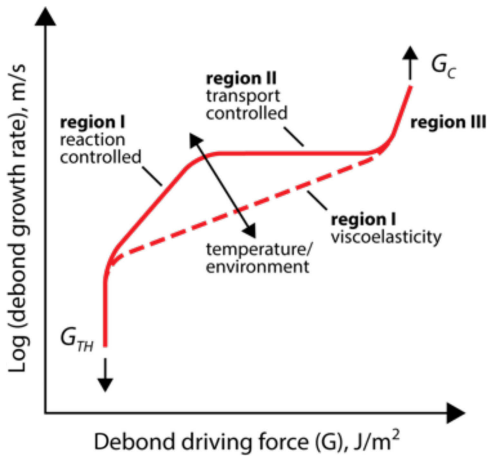

Fig. 1. Schematic subcritical debond curve illustrating the effect of viscoelasticity and chemical reaction associated rate limiting steps on debond growth rate.

Manuscript received June 12, 2018; revised August 20, 2018; accepted October 6, 2018. This work was supported in part by the Alliance for Sustainable Energy, LLC, the manager and operator of the National Renewable Energy Laboratory for the U.S. Department of Energy, under Contract No. DE-AC36-08GO28308 and also by the U.S. Department of Energy's Office of Energy Efficiency and Renewable Energy under Solar Energy Technologies Office Agreement Number 30309. *(Corresponding author: Nick Bosco.)*

N. Bosco is with the National Renewable Energy Laboratory, Golden, CO 80401 USA (e-mail: nick.bosco@nrel.gov).

J. Tracy and R. Dauskardt are with the Stanford University, Stanford, CA 94305 USA (e-mail: jaredmtracy@gmail.com; rhd@stanford.edu).

Color versions of one or more of the figures in this paper are available online at http://ieeexplore.ieee.org.

Digital Object Identifier 10.1109/JPHOTOV.2018.2877436

included in this investigation three formulations of EVA that vary by the relative content of their adhesion promoter, silane: 1) a high-quality EVA with its full complement of silane loading, 0.24 wt%; 2) one formulation containing a reduced silane loading of 0.012 wt%; and 3) one formulation that had no silane added [10]. Measurements of critical and subcritical debonding are made by employing a single cantilever beam method. Experimental results and subsequent analysis with fracture-kinetics modeling indicate that both rising temperature and relative humidity increase the debond growth rate due to viscoelastic effects in the EVA, and at conditions of high humidity and low driving force, a hydrolysis reaction-controlled fracture process emerges.

II. Materials and Methods

A. Materials

Three EVA encapsulants were used to fabricate samples: 1) a pristine material with its full complement of silane loading of 0.24 wt%, which was within its expiration date and properly stored in an air-free, sealed container; 2) a formulation containing a reduced silane loading of 0.012 wt%; and 3) a formulation that had no silane added [10]. These materials are subsequently referred to by their relative amounts of silane loading: 100%, 5%, and 0%, respectively. Samples were fabricated by laminating a silicon wafer to a slide of glass with each encapsulant. The alkaline-textured, monocrystalline Si wafers had received a ~70-nm-thick SiN_x deposition on their faying surface to simulate the antireflective coating (ARC) of a commercial PV product.

To prepare for measurement, a titanium beam (5.0-mm wide, 100-mm long, and 1.6-mm thick) was adhered to the back of each Si wafer with a two-part epoxy. Each beam contained a counter-sunk through a hole at one end to receive a jeweled loading tab. Once the epoxy had fully cured, the Si wafer was sectioned around the beam, and the sample fixtured in the load frame for measurement.

B. Exposures

A preliminary experiment was conducted to characterize G_c of the EVA/Si-PV interface as a function of temperature, prior to and following a 1000-h exposure at 85 °C/ 85% RH. These critical measurements were made in an environmental chamber at 15% RH and six temperatures between 25–80 °C.

All subcritical debond measurements were conducted in an environmental chamber at distinct temperatures and relative humidity conditions that varied between 25–50 °C and 10–90% RH, as described in Table I. There were no preconditioning exposures for these measurements.

C. Metrology

A single cantilever beam method was employed to evaluate debonding at subcritical strain energy release rates [8], [11]. The strain energy release rate (G), is defined as

$$G = \frac{P^2}{2b}\frac{\mathrm{dC}}{da} \tag{1}$$

TABLE I
Environmental Measurement Conditions

Temp	Humidity (%)					
(C)	10	15	30	40	80	90
25	5, 100%	0%	0%	5,100%	5,100%	0%
40	5, 100%	0%				
50	5, 100%	0%				

Values in table are the relative amounts of Silane loading of the EVA formulations.

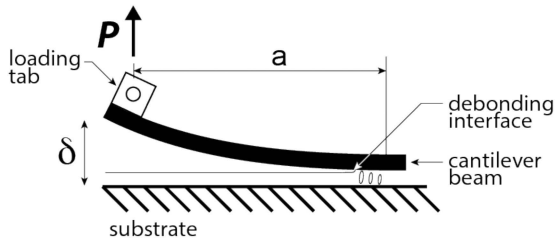

Fig. 2. Schematic of the single cantilever beam method.

where P is the load applied normal to the free end of the cantilever beam, b the beam's width, and dC/da the change in beam compliance, C, with extending debond length, a, see Fig. 2. The critical value of the strain energy release rate, G_c, or debond energy (adhesion), is evaluated by (1) for critical loads, P_C, that result in debond extension.

According to beam theory, compliance of a single cantilever beam is proportional to the cube of its length, therefore (1) may be re-expressed as

$$G = \frac{3P^2}{2b}\mathrm{ma}^2 \tag{2}$$

where m is the proportionality constant between beam compliance and the cube of debond length. A further analysis of beam compliance shows that the debond growth rate (da/dt) for a cantilever beam at a fixed displacement may be expressed as

$$\frac{da}{dt} = -\left(\frac{dP}{dt}\right)_i \frac{ma^3}{3\mathrm{P}_i ma^2} \tag{3}$$

where dP/dt is the instantaneous rate of change in load, P_i the instantaneous load, and a the initial debond length. Plots of subcritical debond growth rate versus the applied driving force (v-G plots) may then be constructed by matching instantaneous load and debond length values between (2) and (3).

Experimentally, a measurement commences by loading the beam at a constant displacement rate of 10 μm/s until the debond begins to propagate. Several load reversals are then conducted to experimentally develop dC/da and determine G_c. Upon final loading, displacement is fixed just below a load value that would further propagate the debond and load recorded with time. The measurement is allowed to proceed at this fixed displacement until debond growth rates on the order 10^{-9} m/s are achieved.

A set of tensile tests was also conducted to elucidate the effect of humidity on the bulk properties of the 100% EVA. For this measurement, the EVA was subjected to the same curing process as those which were fabricated into laminates. The cured, unsupported, films were 440-μm thick and cut into 5-mm strips.

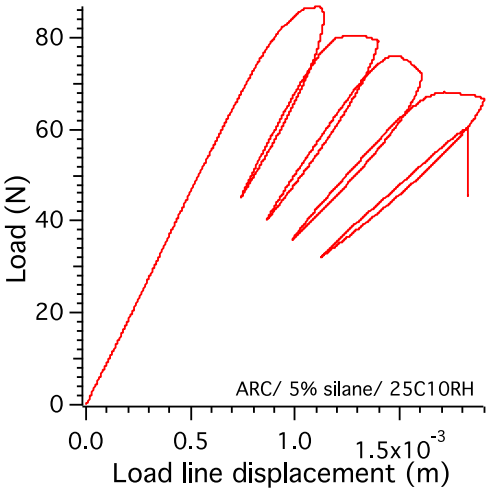

Fig. 3. Representative load versus displacement plot obtained during a v-G measurement. Load reversals are conducted to extract dC/da and obtain Gc values as the debond extends. Drop in load at fixed displacement (∼19 mm) marks the subcritical measurement.

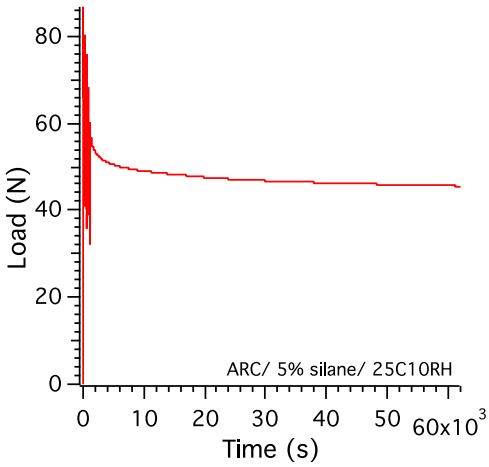

Fig. 4. Representative measurement load versus time plot obtained during a v-G measurement. Decay in load denotes subcritical debonding is occurring.

These strips were fixtured in tensile grips and displaced at a constant strain rate of approximately 0.005/s while load was recorded. Two measurements were made, one at 25 °C/10% RH and one at 25 °C/80% RH.

III. Results

Representative plots that illustrate the measurement and analysis process for subcritical debonding characterization are presented in Figs. 3–7. First, the load versus load-line displacement plot recorded during the measurement demonstrates the repeated load reversals that provide for both extraction of the change in beam compliance, *dC/da*, and repeated measurements of G_c with debond extension (see Fig. 3). Experimental measurements of debond extension are made prior to initial loading and at each load reversal. Measurement load is plotted versus time to illustrate the slow increase in beam compliance, realized as a decreasing load at fixed displacement (∼19 mm), which provides *dP/dt* for calculation of the v-G curve (see Fig. 4).

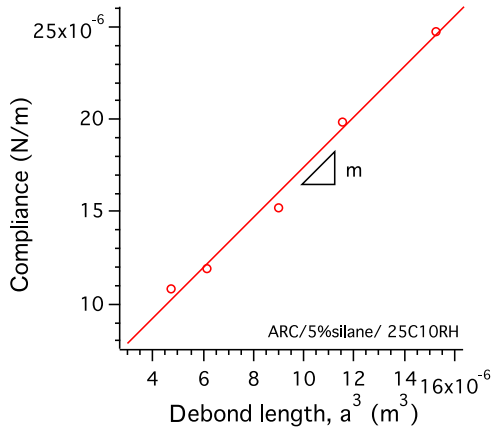

Fig. 5. Compliance (displacement/ load) is plotted for the initial loading and each load reversal versus the cube of debond length. Linear fit provides for the proportionality constant, m, required in (2) and (3).

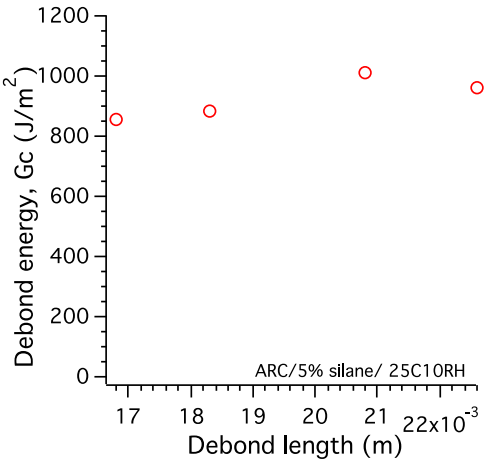

Fig. 6. Representative Gc versus debond length plot. Measurements of peak loads and associated debond lengths (see Fig. 3) and extraction of the proportionality constant (see Fig. 5) provide for a calculation of the critical strain energy release rate as the debond propagates.

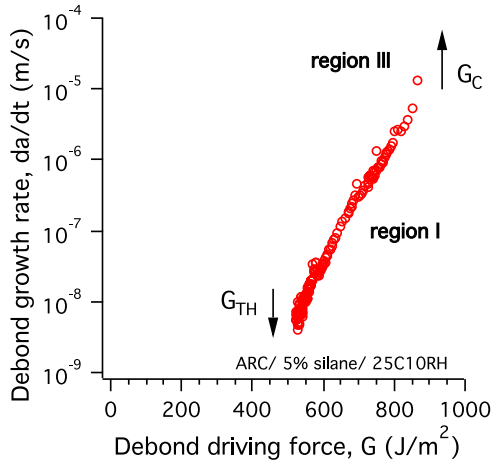

Fig. 7. Representative v-G plot obtained from the measurement and analysis illustrated in Figs. 3–6. Curve is bound by Gc at high debond growth rates, which corresponds to the discrete values in Fig. 6, and Gth at which point the debond arrests. This v-G plot does not exhibit region II behavior.

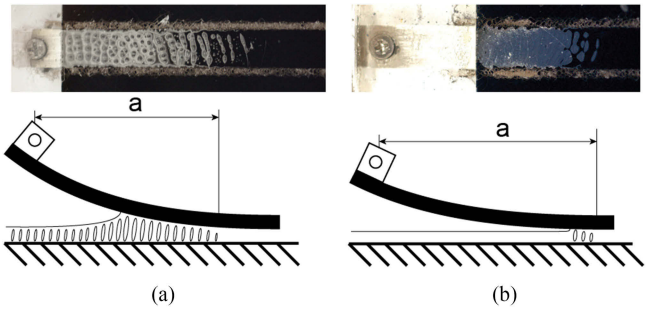

Fig. 8. Optical images through the glass laminate visualizing the delaminated interface and debond front for (a) 100 % EVA with Gc, $>$ 500 J/m^2 and (b) 0% EVA with Gc, $<$ 500 J/m^2. Each image is accompanied by a cartoon illustrating the interpreted character of the failure, associated cohesive zone and measurement of debond length, a.

Plotting the compliance fit (displacement/load) of the initial loading and each load reversal versus the cube of the experimentally measured debond length provides for experimental characterization of *dC/da* through the proportionality constant, *m* (see Fig. 5). Measurements of peak loads from the load versus displacement measurement, associated debond lengths, and the extraction of the proportionality constant provide for a calculation of G_c as the debond propagates (see Fig. 6). Finally, the v-G plot is obtained from the preceding measurements and analysis (see Fig. 7). This representative curve is bound by G_c at high debond growth rates, which corresponds to the discrete values presented in Fig. 6, and G_{TH} at low debond growth rates where the debond arrests. This v-G plot does not exhibit region II behavior.

For all materials and conditions examined, delamination occurs in an apparently adhesive fashion between the Si wafer's ARC and the EVA encapsulant. In samples measured to have G_c values above $\sim$500 J/m^2, the adhesive failure is preceded by substantial cavitation in the EVA prior to debonding, resulting in a large cohesive zone [see Fig 8(a)]. When G_c values are below $\sim$500 J/m^2, the cohesive zone that precedes the debond front shrinks considerably or is absent [see Fig. 8(b)].

A comparison of G_c values measured as a function of temperature or humidity for each EVA are presented in Figs. 9 and 10. Both measurements of the material subject to the 1000-h 85 °C/85% RH exposure and the unexposed material used for the subcritical debonding measurements are included. The 1000-h 85°C/85% RH exposure was not found to degrade G_c when measured as a function of temperature at 15% RH (black curves versus temperature).

The G_c evaluation of the unexposed 100% material yields similar values (red curve versus temperature at 10% RH). The G_c of the EVA formulations with decreased silane content exhibit a significant drop compared to the 100% EVA. For similar environmental conditions, G_c of the 5% EVA drops by a factor of $\sim$2, and of the 0% EVA over an order of magnitude when compared to the 100% EVA. Finally, the G_c evaluation, again measured directly preceding subcritical debonding measurement, made at 25 °C as a function of humidity demonstrates a similar effect of decreasing G_c as temperature increased. This observation suggest that humid air must be present at the debond front to compromise G_c, rather than as a pre-exposure intended to saturate the encapsulant.

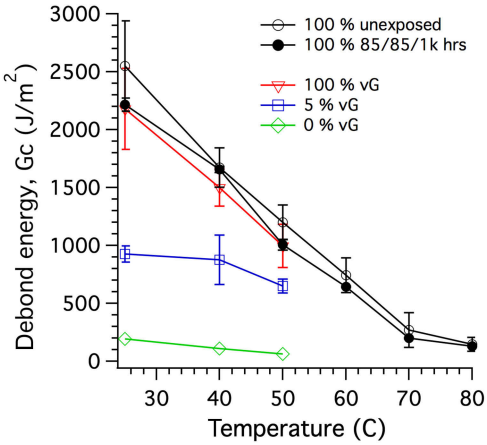

Fig. 9. G_c versus measurement temperature. Both the pre and post1000-h 85 °C/85% RH exposure measurements (black curves) and G_c measurements made during the subcritical analysis are included.

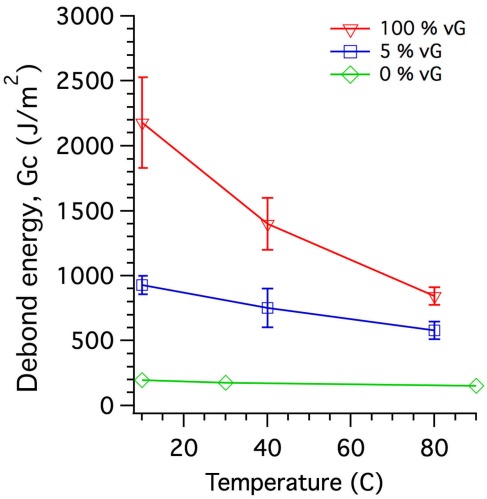

Fig. 10. G_c versus measurement humidity made during the subcritical analysis.

Temperature and humidity series v-G plots for the three materials investigated are presented in Figs. 11–13. All materials demonstrate an acceleration of subcritical debond growth rate with both increasing temperature and humidity. However, while the character of the 100 and 5% EVA temperature and humidity series v-G curves are similar, the 0% EVA exhibits characteristically different v-G responses to temperature and humidity.

The result of the two 100% EVA tensile measurements are presented in Fig. 14. The effect of humidity exhibits a large influence on the rate of the viscoelastic response. Here, the high humidity condition results in a decreased relaxation time.

IV. Analysis

Two fracture kinetics models are used to analyze the subcritical debonding behavior of the three materials investigated to provide an insight into the potential mechanisms responsible for the observed behavior. The application of these models

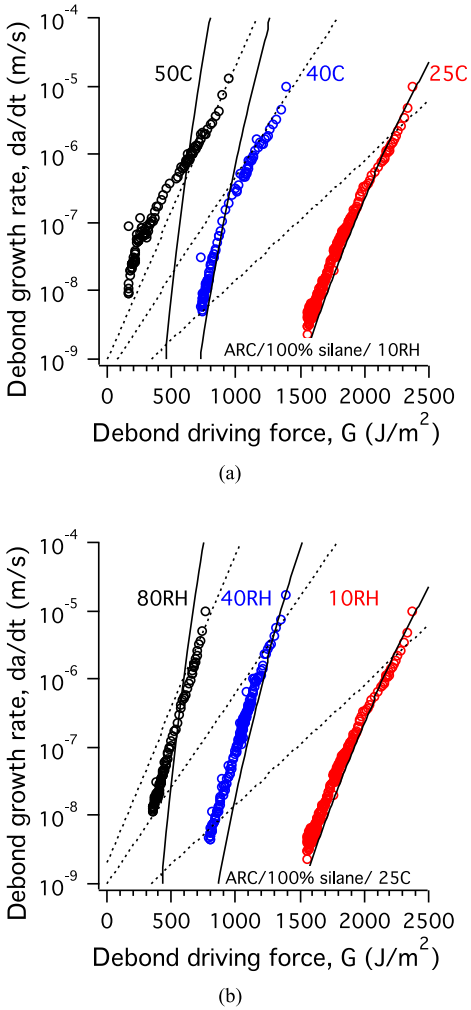

Fig. 11. Debond growth rate for the 100 % EVA measured at (a) 10% RH and 25, 40, and 50 °C, and (b) 25 °C and 10%, 40%, and 80% RH. Included in the plots are best fits of the viscoelastic (solid) and reaction rate (dashed) models.

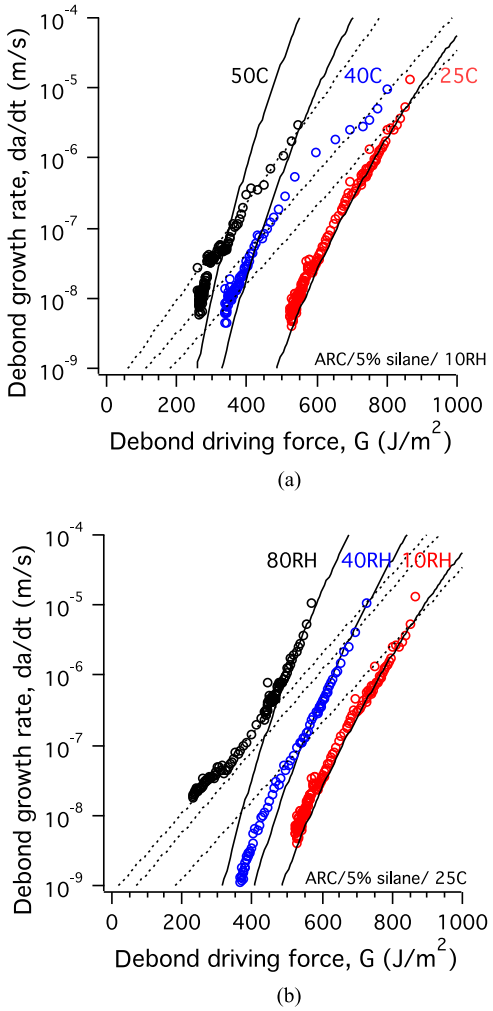

Fig. 12. Debond growth rate for the 5% EVA measured at (a) 10% RH and 25, 40, and 50 °C, and (b) 25 °C and 10%, 40%, and 80% RH. Included in the plots are best fits of the viscoelastic (solid) and reaction rate (dashed) models.

is limited to describe only region I behavior. The first model supports the hypothesis that the debond growth rate, *da/dt*, is proportional to the rate of formation of the viscoelastic zone at the debonding tip and is expressed as

$$\frac{da}{dt} = \alpha \delta_c^{1-1/n} G^{1/n} \exp\left[-\frac{E_a}{R}\left(\frac{1}{T+\gamma \mathrm{RH}} - \frac{1}{T_r}\right)\right] \quad (4)$$

where the prefactor α incorporates the yield strain and time dependent modulus of the encapsulant, δ_c the debond tip opening displacement at $G = G_c$, n a measure of rate sensitivity ($n = 0$ for perfectly elastic solids), G the applied strain energy release rate, E_a the activation energy for the viscoelastic relaxation process, R the universal gas constant, T temperature, T_r a reference temperature, RH the relative humidity, and γ the RH to T equivalence in bonding kinetics [9], [12], [13]. Note that this model considers that the debond kinetics are dictated exclusively by the bulk material properties of the encapsulant and that the effect of increasing RH is directly proportional to the effect of increasing temperature.

The second model considers the fracture process as a chemical reaction to support the hypothesis that the observed subcritical debonding behavior is a manifestation of a hydrolysis reaction occurring at the debond front. In this case, the region I debonding rate is considered proportional to the rate of reaction and expressed as

$$\frac{da}{dt} = \mathrm{A} \exp\left(-\frac{E}{RT}\right)\left(\frac{P_{H_2O}}{P^0}\right)^n \exp\left(\frac{bG}{RT}\right) \quad (5)$$

where E is the stress free activation energy, P_{H2O} the partial pressure of water vapor, P^0 the standard state pressure (1 atm), n the order of reaction, b an activation area related to the activation volume at the debond front, G the applied strain energy release rate, R the universal gas constant, and T temperature [14], [15]. A frequency factor is incorporated into the pre-exponential constant, A. Note that this model was originally developed for bulk glass systems where the activation volume, related to b, is not a function of temperature. When applied to the current system where a viscoelastic solid, EVA, is present at the debond tip, it is reasonable to expect that the activation volume does scale with temperature and was therefore treated as a fitting parameter in the present analysis.

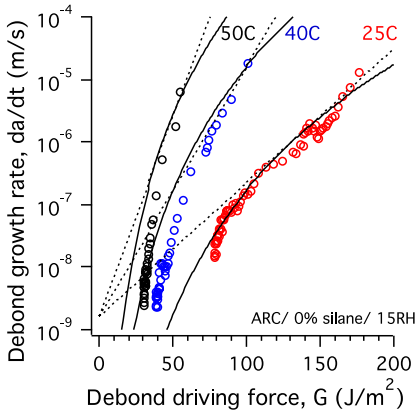

(a)

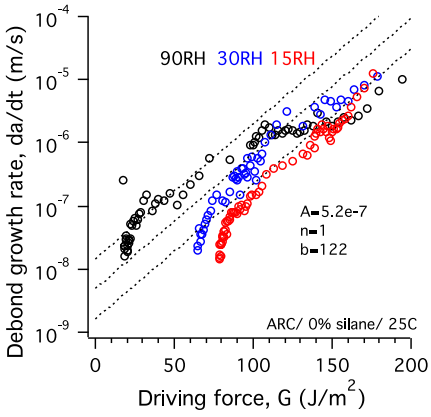

(b)

Fig. 13. Debond growth rate for the 0% EVA measured at (a) 15% RH and 25, 40, and 50 °C, and (b) 25 °C and 15%, 30%, and 90% RH. Included in the plots are best fits of the viscoelastic (solid) and reaction rate (dashed) models.

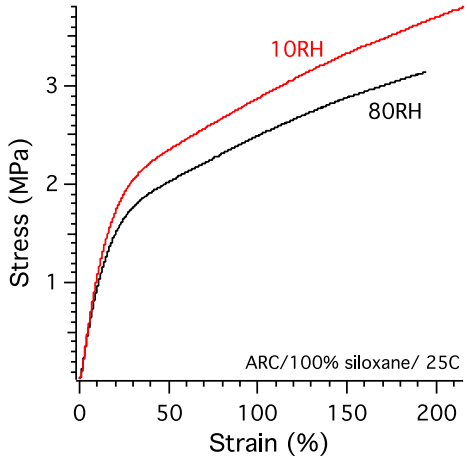

Fig. 14. Tensile measurements of the 100% EVA material at 25 °C and 10%, 80% RH.

The best fits of the viscoelastic ((4), solid curves) and reaction rate ((5), dashed curves) models are presented in Figs. 11–13. For clarity, all models span the full range of G, yet should only be interpreted for their ability to fit region I behavior. For the 100% EVA, the viscoelastic debonding model was found to best describe the observed fracture kinetics when the parameters α, n, E_a, and γ were used to fit the data ($E_a = 795$ kJ/mol, $n = 0.049$, $\gamma = 0.38$ K/%). The utility of this model, especially for the humidity series, is consistent with the result of the conducted tensile test where increasing humidity had the effect of decreasing stress relaxation time. While most curves fit exceptionally well with this model, the 50 °C/ 10% RH condition demonstrates an unexpected acceleration of debond growth rate not anticipated by the model. The reaction rate model was found to better fit the relevant portions of the 40 °C/ 10% RH and 50 °C/ 10% RH conditions as well as the 25 °C/ 80% RH conditions when the parameters A and b were used to fit the data for a first order reaction ($n = 1$). Typically, application of a reaction rate model is predicated on the presence of a G insensitive transport-controlled region II, which is notably absent from these curves. However, unlike the inorganic elastic solids for which these models were originally developed, the current EVA systems exhibit an extraordinarily large debond tip opening displacement that may circumvent the emergence of region II behavior. This combination of fits suggests that a bulk change in the viscoelastic properties of the EVA dominates the debond kinetics at high G and low humidity and the effect of a chemical reaction only becomes apparent at higher humidity and lower values of G.

The combination of fits is similar for the 5% EVA for both the viscoelastic ($E_a = 307$ kJ/mol, $n = 0.066$, $\gamma = 0.23$ K/%) and reaction rate models ($n = 1$). Here too, the viscoelastic model fits the high G-low humidity data best, but fails to accurately capture the behavior of the low G-high humidity conditions.

Finally, for the 0% EVA, there is a clear departure from the viscoelastic debonding model for the humidity series. Here, a distinct reaction-controlled region emerges and well fits with (5) for a first-order reaction and, in this case, considering a constant activation volume, b. While the viscoelastic model was not capable of fitting the humidity series and was thus omitted from the plot, it was able to describe the temperature series behavior well ($E_a = 236$ kJ/mol, $n = 0.15$). This combination of fits follows those for the previous two materials where the viscoelastic model is more capable of describing the behavior of low humidity debond growth rates.

V. Conclusion

The effect of temperature and humidity on the critical debond energy and debonding kinetics of EVA with various silane contents was evaluated. An EVA formulated with its requisite silane content (100% EVA) did not exhibit a degradation of its critical debond energy, G_c, following a 1000-h exposure at 85 °C/85% RH. When similar, unexposed materials were measured in an environment of either increased temperature or humidity, however, G_c was dramatically reduced. This observation suggests that humid air must be present at the debond front, rather than as a pre-exposure intended to saturate the encapsulant, to compromise G_c. G_c was also found to dramatically decrease with reduced silane content. For similar environmental conditions, G_c of EVA formulated with 5% of its requisite silane content drops by a factor of ~2, and that of

EVA with no silane drops by over an order of magnitude when compared to the 100% EVA. All materials also demonstrate an acceleration of subcritical debond growth rate with both increasing temperature and humidity.

Two previously established models for debonding kinetics were employed to study the results of subcritical debonding measurements, one based on the viscoelastic behavior of the encapsulant and one on the rate of stress-enabled hydrolysis at the debond front. The viscoelastic model was found to fit the high G, low humidity data best but failed to accurately capture the behavior of the low G, high humidity conditions. The low G, high humidity conditions were best fit with the reaction rate model when the activation area at the debond tip was also used as a fitting parameter. This combination of fits suggests that a bulk change in the viscoelastic properties of the EVA dominates the debond kinetics at high G and low humidity and the effect of a chemical reaction only becomes apparent at higher humidity and lower values of G. This conclusion is supported well by the unique behavior of the relatively weak 0% EVA where the humidity series only fits with the reaction rate model.

ACKNOWLEDGMENT

This work was authored in part by Alliance for Sustainable Energy, LLC, the manager and operator of the National Renewable Energy Laboratory for the U.S. Department of Energy (DOE) under Contract No. DE-AC36-08GO28308. Funding provided by the U.S. Department of Energy's Office of Energy Efficiency and Renewable Energy (EERE) under Solar Energy Technologies Office (SETO) Agreement Number 30309. The views expressed in the article do not necessarily represent the views of the DOE or the U.S. Government. The U.S. Government retains and the publisher, by accepting the article for publication, acknowledges that the U.S. Government retains a nonexclusive, paid-up, irrevocable, worldwide license to publish or reproduce the published form of this work, or allow others to do so, for U.S. Government purposes.

REFERENCES

[1] J. Tracy, N. Bosco, and R. H. Dauskardt, "Evaluation of encapsulant adhesion to surface metallization of photovoltaic cells," *IEEE J. Photovolt.*, vol. 7, no. 6, pp. 1635–1639, Nov. 2017.

[2] N. Bosco, J. Tracy, S. Kurtz, and R. H. Dauskardt, "Defining threshold values of encapsulant and backsheet adhesion for PV module reliability," *IEEE J. Photovolt.*, vol. 7, no. 6, pp. 1536–1540, Nov. 2017.

[3] J. Tracy, N. Bosco, F. D. Novoa, and R. H. Dauskardt, "Encapsulant and backsheet adhesion metrology for photovoltaic modules," *Prog. Photovolt.*, vol. 25, pp. 87–96, 2016.

[4] N. Bosco, J. Tracy, R. H. Dauskardt, and S. Kurtz, "Development and first results of the width-tapered beam method for adhesion testing of photovoltaic material systems," in *Proc. IEEE Photovolt. Spec. Conf.*, Portland, OR, USA, 2016, pp. 0106–0110.

[5] D. C. Jordan, J. Wohlgemuth, and S. Kurtz, "Technology and climate trends in PV module degradation," in *Proc. 27th Eur. Photovolt. Solar Energy Conf.*, 2012, pp. 2411–2415.

[6] T. Shioda, "Short-term and long-term field failures related to PV encapsulants in Japan," in *Proc. 2nd Int. Workshop Sustain. Actions "Year by Year Aging" Under Rel. Investigations Photovolt. Modules*, Otsu, Japan, 2017.

[7] W. Bradley, W. J. Cantwell, and H. H. Kausch, "Viscoelastic creep crack growth: A review of fracture mechanical analyses," *Mech. Time-Dependent Mater.*, vol. 1, no. 3, pp. 241–268, Sep. 1, 1997.

[8] R. P. Birringer, R. Shaviv, P. R. Besser, and R. H. Dauskardt, "Environmentally assisted debonding of copper/barrier interfaces," *Acta Materialia*, vol. 60, no. 5, pp. 2219–2228, 2012.

[9] F. D. Novoa, D. Miller, and R. H. Dauskardt, "Adhesion and debonding kinetics of photovoltaic encapsulation in moist environments," *Prog. Photovolt.: Res. Appl.*, vol. 24, pp. 183–194, 2016.

[10] J. L. Koenig, J. F. Boerio, E. P. Plueddemann, J. Miller, P. B. Willis, and E. F. Cuddihy, "Chemical bonding technology: Direct investigation of interfacial bonds," Tech. Rep. NASA-CR-176657, Jet Propulsion Lab., California Inst. Tech., Pasadena, CA, USA, 1986.

[11] R. H. Dauskardt, M. Lane, Q. Ma, and N. Krishna, "Adhesion and debonding of multi-layer thin film structures," *Eng. Fracture Mech.*, vol. 61, no. 1, pp. 141–162, 1998.

[12] F. D. Novoa, D. C. Miller, and R. H. Dauskardt, "Debonding kinetics of photovoltaic encapsulation in moist environments," *Prog. Photovolt.: Res. Appl.*, vol. 24, pp. 183–194, 2016.

[13] F. D. Novoa, D. C. Miller, and R. H. Dauskardt, "Environmental mechanisms of debonding in photovoltaic backsheets," *Sol. Energy Mater. Sol. Cells*, vol. 120, pp. 87–93, 2014.

[14] S. M. Wiederhorn, E. R. Fuller, and R. Thomson, "Micromechanisms of crack growth in ceramics and glasses in corrosive environments," *Metal Sci.*, vol. 14, nos. 8/9, pp. 450–458, 1980.

[15] S. Y. Kook and R. H. Dauskardt, "Moisture-assisted subcritical debonding of a polymer/metal interface," *J. Appl. Phys.*, vol. 91, no. 3, pp. 1293–1303, Feb. 2002.

Authors' photographs and biographies not available at the time of publication.